Figure 10. Distributions of Σ_{Ld} (left panel), Σ_{Md} (middle), and Σ_{Ld}/Σ_{Md} (right) for all galaxies. The cutoffs at low Σ_{Ld} and low Σ_{Md} are due to limitations in sensitivity. The total dust luminosity $L_{\rm d}$ is contributed mainly by higher surface brightness pixels, with $\Sigma_{Ld} \approx 10^8 L_\odot\,{\rm kpc}^{-2}$. The total mass is contributed mainly by pixels with $\Sigma_{Md} \approx 10^{5.2} M_\odot\,{\rm kpc}^{-2}$, corresponding to extinction $A_V \approx 1\,{\rm mag}$. The right panel shows that most of the dust has $L_{\rm d}/M_{\rm d} \approx 150 L_\odot/M_\odot$, corresponding to a heating rate $\overline{U} \approx 1$.
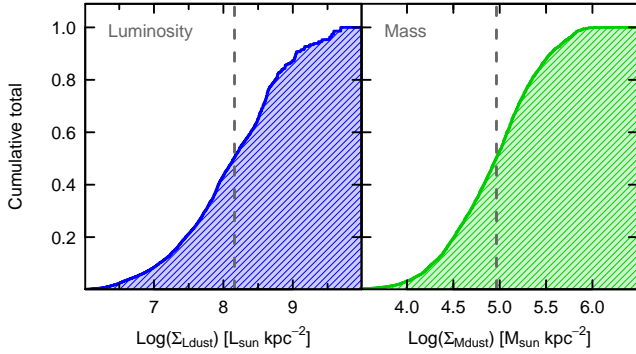

Figure 11. Cumulative distributions of dust luminosity $L_{\rm d}$ (left panel) and dust mass $M_{\rm d}$ (right panel) for all galaxies. The vertical dashed lines show the surface brightness Σ_{Ld} and surface density Σ_{Md} above and below which provides 50% of the total **dust** luminosity and **dust** mass, respectively: $\Sigma_{Ld} = 10^{8.2} L_\odot\,{\rm kpc}^{-2}$; and $\Sigma_{Md} = 10^{5.1} M_\odot\,{\rm kpc}^{-2}$. The regions with $\Sigma_{Ld} > 10^{8.2} L_\odot\,{\rm kpc}^{-2}$ comprise $\sim$3% of the pixels, and those with $\Sigma_{Md} > 10^{5.1} M_\odot\,{\rm kpc}^{-2}$ $\sim$22% of the pixels.

$10^{8.2} L_\odot\,{\rm kpc}^{-2}$ and $\Sigma_{Md} = 10^{5.1} M_\odot\,{\rm kpc}^{-2}$. Regions with dust light and mass surface densities greater than these values comprise only a small fraction of the total; from Fig. 10 we see that 50% of the dust light comes from only $\sim$3% of the (brightest) pixels, and 50% of the total dust mass from $\sim$22% of the (densest) pixels.

In what follows we have applied a limit in dust surface brightness $\Sigma_{Ld} \geq 2 \times 10^6 L_\odot\,{\rm kpc}^{-2}$; thus the low signal-to-noise faint outer regions of the sample galaxies (where estimates of parameters such as Σ_{Md} and $q_{\rm PAH}$ may become unreliable) will not be considered. As seen above,

such regions contribute very little to either the light budget or the mass budget of the dust over the sample as a whole. Applying such a cut ensures that the plotted DL07 parameters (and the photometric quantities) will be as accurate as possible, given the constraints of the data; the total number of $18'' \times 18''$ pixels in the sample is reduced to $\sim$25 500.

We now investigate the IR observational signatures associated with dust heating ($U_{\min}$). Figure 12 shows $U_{\min}$ for all galaxies plotted versus MIPS and SPIRE flux density ratios, f_{70}/f_{160}, f_{70}/f_{250}, and f_{160}/f_{500}. Because of the unexplained discrepancies between MIPS and PACS photometry (see Figure 2), we have elected to use only MIPS photometry for f_{70} and f_{160}. The left panel shows that the flux ratio f_{70}/f_{160} is not a very good predictor of $U_{\min}$. This is because when $U_{\min} \lesssim 1$, the $70\,\mu{\rm m}$ emission has an appreciable contribution from (1) single-photon heating of small grains, and (2) dust in regions with high starlight intensities (assuming $\gamma > 0$, which is almost always the case). The flux ratio f_{160}/f_{250}, shown in the middle panel, ameliorates the potential domination of the emission by small-grain stochastic heating, but the wavelength ratio of the two fluxes is insufficient to reliably sample $U_{\min}$; a small range in flux ratio corresponds to as much as an order of magnitude change in $U_{\min}$. However, the right panel shows that the f_{160}/f_{500} flux ratio correlates quite well with $U_{\min}$ because the emission at both $160\,\mu{\rm m}$ and $500\,\mu{\rm m}$ is dominated by the larger grains heated by starlight intensities near $U_{\min}$. Because $160\,\mu{\rm m}$ is not in the Rayleigh-Jeans limit for the grain temperatures in these galaxies, the f_{160}/f_{500} ratio is sensitive to large-grain temperature, and hence to starlight heating rate. The best-fit correlation, obtained with median clipping and a "robust" regression algorithm, effective for minimizing the effects of outliers
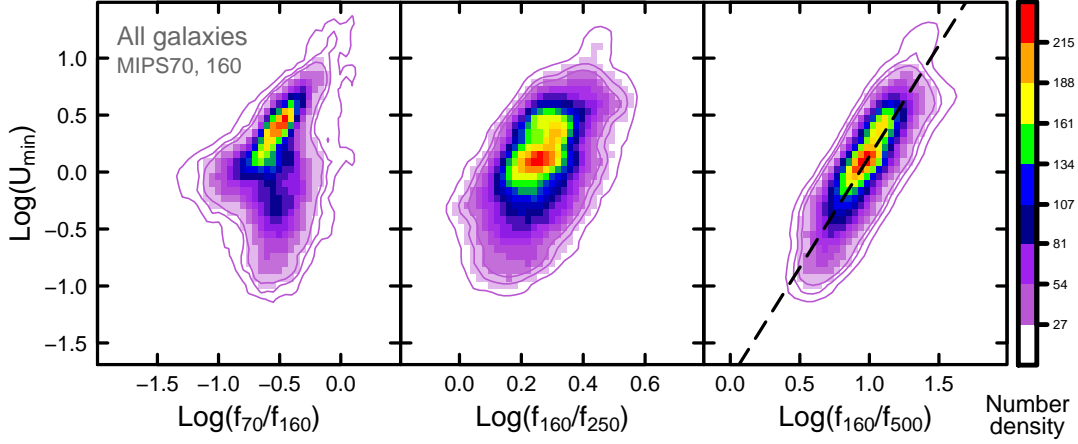
Figure 12. Minimum starlight heating intensity $U_{\min}$ vs. f_{70}/f_{160} (left panel), f_{160}/f_{250} (middle), and f_{160}/f_{500} (right) for all galaxies. The 70 and 160μm flux densities f_{70} and f_{160} are from MIPS only (see text). The color coding corresponds to number density of pixels as shown by the rightmost color table. The left panel shows that f_{70}/f_{160} is not a good indicator of $U_{\min}$, because f_{70} is sensitive to both single-photon heating and the emission from dust exposed to starlight intensities $U > U_{\min}$. The middle panel with f_{160}/f_{250} avoids using f_{70}, but the wavelength range is insufficient to adequately sample $U_{\min}$ and a luminosity-weighted dust temperature. Instead, the right panel shows the tight correlation between $U_{\min}$ and f_{160}/f_{500} (the dashed line is Eq. 22), illustrating the close relationship between the minimum heating intensity and the coolest dust.
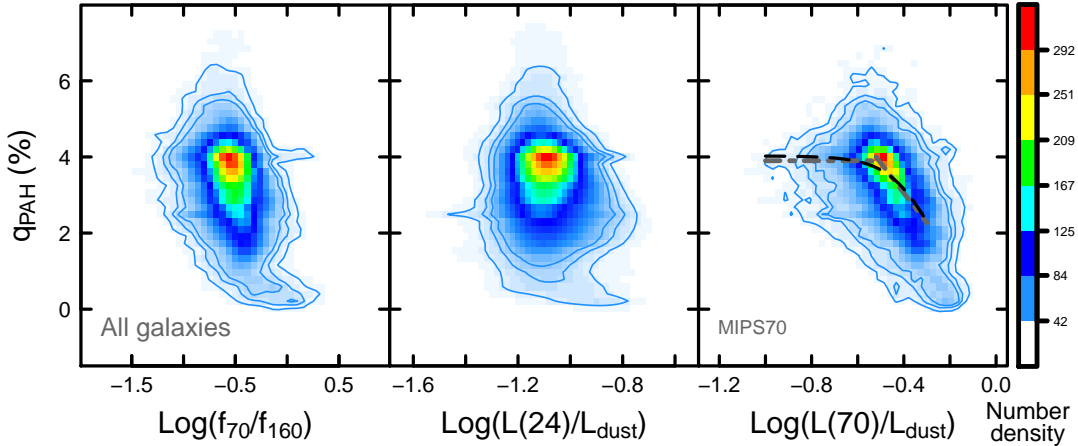
Figure 13. PAH fraction q_{PAH} versus f_{70}/f_{160} (left panel), $\nu L_{24\mu\mathrm{m}}/L_{\mathrm{d}}$ (middle) and $\nu L_{70\mu\mathrm{m}}/L_{\mathrm{d}}$ (right) for all galaxies. The 70 and 160μm flux densities f_{70} and f_{160} are from MIPS only (see text). The color coding corresponds to number density of pixels as shown by the rightmost color table. The trend in the right panel for q_{PAH} to decrease with increasing $\nu L_{24\mu\mathrm{m}}/L_{\mathrm{d}}$ reflects the power of $\nu L_{70\mu\mathrm{m}}/L_{\mathrm{d}}$ to trace q_{PAH}. The (black) long-dashed line represents the best-fit function given in Eq. (23) with rms residuals of $\sim1.2\%$ on q_{PAH}; similar residuals are given by the (grey) dashed-dotted line, a broken power-law fit as given in Eq. (24).

(R Core Team 2014), is given by:

$$\log_{10}(U_{\min}) = (-1.81\pm0.01)+(1.95\pm0.01)\log_{10}\left(\frac{f_{160}}{f_{500}}\right). \tag{22}$$

This relation predicts $U_{\min}$ to within $0.21\,\mathrm{dex}$ **(rms)** over a range of $U_{\min}$ of more than two orders of magnitude. Because the emission at these wavelengths is dom-

inated completely by large grains, this long-wavelength ratio predicts very well the minimum starlight heating intensity.

The PAH abundance parameter q_{PAH} varies from galaxy to galaxy, as discussed in Section 6.5, where it is apparent that there is a correlation between q_{PAH} and the gas-phase metallicity O/H. q_{PAH} also exhibits significant variations within individual galaxies, as can be
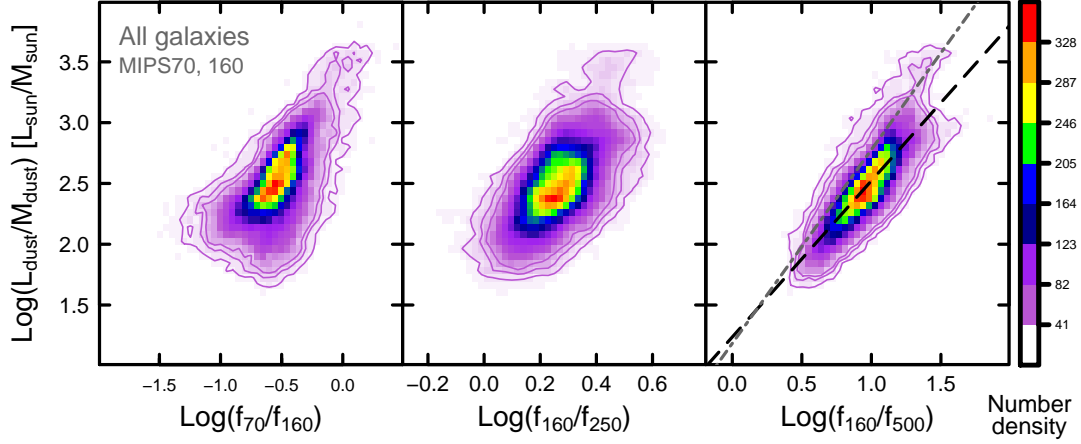
Figure 14. Dust mass-to-light ratio L_d/M_d vs. f_{70}/f_{160} (left panel), f_{160}/f_{250} (middle), and f_{160}/f_{500} (right) for all galaxies. The color coding corresponds to pixel number density as shown by the rightmost color table. The best-fit (robust) regression for f_{160}/f_{500} is shown as a (black) long-dashed line, and corresponds to rms residuals of ~ 0.18 dex (see Eq. 25). The (grey) dashed-dotted line is the analogous best-fit regression for only IC 2574 and NGC 2146 (with 383 dof, see Fig. 15).
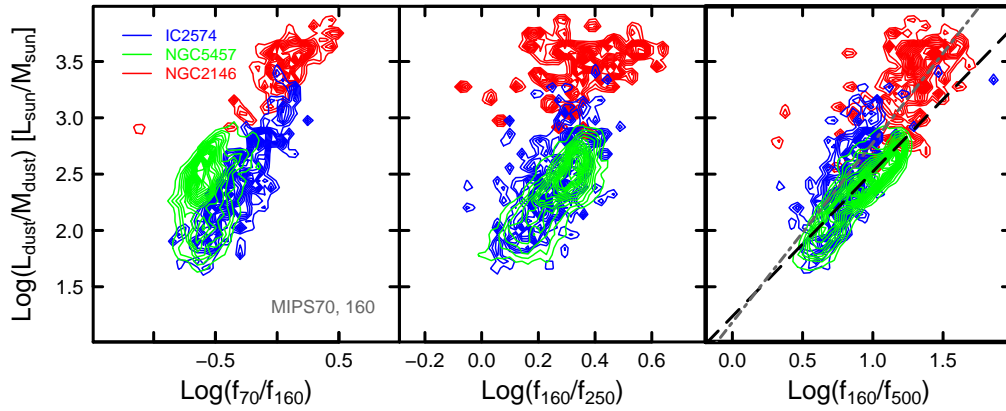
Figure 15. Dust mass-to-light ratio L_d/M_d plotted against f_{70}/f_{160} (left panel) f_{160}/f_{250} (middle), and f_{160}/f_{500} (right) for three galaxies separately: IC 2547, a low-metallicity dwarf; NGC 5457 (M 101), a large grand-design spiral; and NGC 2146, a LIRG. The contours reflect the individual galaxies (IC 2547 blue, NGC 5457 green, and NGC 2146 red), and correspond to pixel number densities. In the right panel, the (black) long-dashed line corresponds to the best-fit regression reported in Fig. 14 for the sample as a whole [see Eq. (25)], and the (grey) dashed-dotted line corresponds to the analogous best-fit regression for only IC 2574 and NGC 2146 (383 dof).

seen from the map of q_{PAH} in M101 (see Fig. 5) as well as for other well-resolved galaxies (see Figs. 17.1-17.62). If q_{PAH} is sensitive to metallicity, then we may expect radial variations within galaxies, with q_{PAH} generally declining with radius. However, our q_{PAH} maps also exhibit substantial azimuthal variations, suggesting that the PAH abundance responds to changes in environmental conditions beyond metallicity alone.

In Fig. 13, we explore – using three different proxies for the starlight intensity – whether q_{PAH} is affected by the intensity of the radiation field. The left panel in Fig. 13 indicates that q_{PAH} seems to be relatively in-

dependent of variations in the f_{70}/f_{160} flux ratio. The f_{70}/f_{160} flux ratio is apparently not uniquely tracing the temperature of the larger grains; as seen in Fig. 12, and discussed below, this ratio begins to reflect U_{min}, and thus large-grain temperature, only above a certain U_{min} threshold ($U_{min} \gtrsim 0.5$). The middle panel, shows little correlation between q_{PAH} and $\nu L_\nu(24\mu m)/L_{dust}$, but the right panel shows a stronger trend where q_{PAH} tends to fall significantly when $\nu L_\nu(70\mu m)/L_{dust}$ rises to the highest levels. The lack of dependence on the $L(24)/L_d$ ratio (and the relatively small 0.5 dex range in $L(24)/L_d$) arises because single-photon heating gener-

ally dominates at $24\,\mu$m; big grains only get hot enough to radiate at $24\,\mu$m when the radiation field is extremely intense. Instead, at $70\,\mu$m, single-photon heating makes a significant contribution only for $U_{\min} \lesssim 0.5$. Thus $L(70)/L_{\rm d}$ is a better indicator of warm large grains than $L(24)/L_{\rm d}$, and it is these warm large grains that are the signature of high-intensity radiation fields that could be associated with PAH destruction.

As seen in the right panel of Fig. 13, the PAH fraction appears to vary with $L(70)/L_{\rm dust}$ according to the empirical relation

$$q_{\rm PAH} \approx \frac{0.0402}{1 + 15\,[L(70)/L_{\rm dust}]^{4.4}} \quad . \qquad (23)$$

where the normalization constant 0.0402 corresponds to $q_{\rm PAH} \approx 4.0\%$; the root-mean-square (rms) residual of this fit is 1.2% on $q_{\rm PAH}$. A similar empirical fit is given by the broken power-law shown by the grey dashed-dotted line in Fig. 13:

$$q_{\rm PAH} \approx \begin{cases} 0.039 & \text{if } \log_{10}(\frac{L70}{L_{\rm dust}}) \leq -0.52 \\ 0.3 - 7.0\log_{10}(\frac{L70}{L_{\rm dust}}) & \text{if } \log_{10}(\frac{L70}{L_{\rm dust}}) > -0.52 \end{cases} \qquad (24)$$

Such a trend may reflect a tendency for PAH destruction to occur in star-forming regions, where O stars supply high energy photons that photodestroy PAHs, and a significant fraction of the dust is exposed to starlight intensities high enough to elevate the $L(70)/L_{\rm dust}$ ratio. Many studies have previously noted suppression of PAH emission in H II regions (e.g., Giard et al. 1994; Helou et al. 2004; Povich et al. 2007; Relaño et al. 2016). In a detailed study of PAH abundances in the Magellanic Clouds, Chastenet et al. (2019) show that $q_{\rm PAH}$ is reduced in regions close to sources of H-ionizing radiation.

High values of $L(70)/L_{\rm d}$ also occur in low-metallicity galaxies, because of radiative transfer effects (hotter stars, less dust attenuation), and is consistent with the tendency for lower $q_{\rm PAH}$ in a metal-poor ISM.

6.7.1. *The resolved dust light-to-mass ratios*

The dust light-to-mass ratio in galaxies and within galaxies, $L_{\rm d}/M_{\rm d}$, should reflect the peak and spread of luminosity-weighted dust temperatures. In the DL07 model, $\overline{U} \propto L_{\rm d}/M_{\rm d}$, so $\overline{U}$ also probes dust temperatures. We would thus expect $L_{\rm d}/M_{\rm d}$ to depend on photometric flux ratios, as long as the two wavelengths in the flux ratios are sampling a sufficiently broad spectral range to be sensitive to large-grain temperature variations. Figure 14 illustrates the correlations in the resolved pixels of all galaxies between Σ_{Ld}/Σ_{Md} (noted as $L_{\rm d}/M_{\rm d}$ in the ordinate axis label) and, as in Fig. 12, three flux density ratios, f_{70}/f_{160}, f_{160}/f_{250}, and f_{160}/f_{500}. The longer the wavelength ratio (in this case $160\,\mu$m$/500\,\mu$m), the better that Σ_{Ld}/Σ_{Md} can be predicted from observations. The right panel (black long-dashed line) of Fig.

14 shows the correlation with f_{160}/f_{500} given by:

$$\log_{10}\left(\frac{L_{\rm d}/M_{\rm d}}{L_\odot/M_\odot}\right) = (1.24\pm0.01)+(1.28\pm0.01)\log_{10}\left(\frac{f_{160}}{f_{500}}\right). \qquad (25)$$

This fit with f_{160}/f_{500} has a rms deviation of 0.16 dex over $>22\,000$ degrees of freedom. The trend of $L_{\rm d}/M_{\rm d}$ with f_{160}/f_{250} is much less reliable, so we have not shown any regression in the middle panel of Fig. 14. Because of the limited wavelength lever arm for the f_{160}/f_{250} flux ratio (see also Fig. 12), for a given f_{160}/f_{250} ratio, $L_{\rm d}/M_{\rm d}$ can vary by a factor of 30 or more; this makes it difficult to accurately determine the dust light-to-mass ratio from f_{160}/f_{250}. Nevertheless, if we know the dust luminosity $L_{\rm d}$, and have a measure of a flux around the peak of dust emission (e.g., f_{160}), and one sufficiently far away and in the Rayleigh-Jeans regime (e.g., f_{500}), we can estimate the dust mass $M_{\rm d}$ to within $\sim$50%.

Fig. 15 shows the same quantities but separately for three galaxies representative of the extremes probed by the KINGFISH sample: IC 2574, a metal-poor dwarf; NGC 5457 (M 101), a face-on grand-design spiral; and NGC 2146, a luminous IR galaxy (LIRG). For a flux density ratio with short+long wavelengths (e.g., f_{70}/f_{160}) the $L_{\rm d}/M_{\rm d}$ ratio within these galaxies can differ by up to an order of magnitude. As has been seen in previous figures, because f_{70}/f_{160} is sensitive to both single-photon heating and the possible exposure of a small fraction of the dust to starlight intensities $U > U_{\min}$, the f_{70}/f_{160} ratio does not strongly constrain the temperature of the dust grains that dominate the total emission. Instead, the longer-wavelength ratio (e.g., f_{160}/f_{500}) is a much better indicator of large-grain temperature, and consequently better correlated with the dust light-to-mass ratio $L_{\rm d}/M_{\rm d}$. Two regressions are shown in Figs. 14 and 15; the (black) long-dashed line, described above [see Eq. (25)], is for the entire sample. The (grey) dashed-dotted one is the regression obtained for only IC 2574 and NGC 2146, and given by:

$$\log_{10}\left(\frac{L_{\rm d}/M_{\rm d}}{L_\odot/M_\odot}\right) = (1.18\pm0.05)+(1.59\pm0.04)\log_{10}\left(\frac{f_{160}}{f_{500}}\right). \qquad (26)$$

The regression for the entire sample is entirely consistent with NGC 5457 (M 101), but not for IC 2574 and NGC 2146, which may be considered two "extreme" galaxies. The overall radiation fields $\overline{U}$ in IC 2574 and NGC 2146 are higher (in the mean, by $\sim$40% and a factor of 13, respectively) than that of NGC 5457. These more intense heating fields, possibly a signature of starbursts, result in a slightly steeper slope relating $L_{\rm d}/M_{\rm d}$ and f_{160}/f_{500} than in more quiescent environments such as the disk of NGC 5457 (and most of the KINGFISH sample).

In the present model, the dust temperatures are determined by the starlight intensity distribution within a
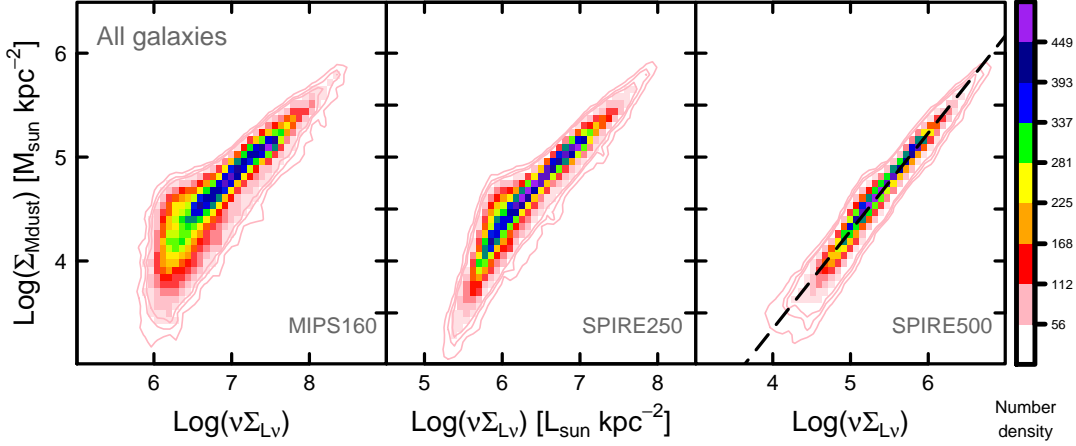
Figure 16. Dust-mass surface density Σ_{Mdust} versus monochromatic surface brightness $\nu\Sigma_{L_\nu} = 4\pi\nu I_\nu$ in the MIPS 160 μm (left panel), SPIRE 250μm (middle), and SPIRE 500μm (right) bands, for all galaxies. The color coding corresponds to pixel number density as shown by the rightmost color table. The dashed line in the right panel (SPIRE500) shows the best-fit regression relating dust mass surface density Σ_{Mdust} to 500μm luminosity surface density $\nu\Sigma_{L_\nu}(500\mu m)$ (Eq. 27). See Sect. 6.7.2 for more details.

pixel, which is characterized by three parameters: $U_{\min}$, γ, and α (see Section 5), and we need more than two bands if we wish to determine the distribution of temperatures for the emitting dust well enough to reliably estimate the mass of dust in the pixel. On the other hand, if flux ratios at longer wavelengths are considered (right panel of Fig. 15), there is much less variation within and between galaxies. Such behavior was also seen with $U_{\min}$ in Fig. 12, and suggests that ratios at these longer wavelengths better trace $L_{\mathrm{d}}/M_{\mathrm{d}}$, because they provide better information about the temperatures of the large grains that dominate the dust luminosity.

6.7.2. *The resolved dust mass surface densities*

Given the relative constancy of dust-to-metals ratios for galaxies with metallicities $12 + \log_{10}(\mathrm{O/H}) \gtrsim 8.4$ (see Fig. 8b), the dust luminosity in the Rayleigh-Jeans (R-J) regime of the dust SED has become a popular tracer of ISM mass (e.g., Corbelli et al. 2012; Eales et al. 2012; Groves et al. 2015; Scoville et al. 2014, 2016, 2017). This is an effective technique both locally and at high redshift because the R-J tail of the dust emission probes optically-thin dust, and is relatively insensitive to dust temperature. Here we explore whether this is also true for the spatially-resolved dust emission in the KING-FISH sample. Figure 16 shows the dust mass surface density $\Sigma_{M_{\mathrm{d}}}$ (estimated from the renormalized DL07 model) plotted against monochromatic dust luminosity surface density $\Sigma_{\nu L_\nu} = 4\pi\nu I_\nu$, in the MIPS 160 μm, SPIRE 250 μm, and SPIRE 500 μm bands. It can be seen that at 160 μm, a wavelength that generally probes the dust emission peak, there is only a broad correlation with more than an order of magnitude dispersion at low surface brightness. As wavelength increases toward the SPIRE bands, the correlation improves, and becomes

very good at 500 μm, similar to the trends found for KINGFISH global values by Groves et al. (2015).

The rightmost panel reports the best-fit correlation, obtained with the robust regression algorithm:

$$\log_{10}\left(\frac{\Sigma_{M_{\mathrm{dust}}}}{M_\odot\,\mathrm{kpc}^{-2}}\right) =$$

$$(-0.42 \pm 0.01) + (0.942 \pm 0.001)\log_{10}\left(\frac{\Sigma_{\nu L_\nu(500\mu m)}}{L_\odot\,\mathrm{kpc}^{-2}}\right) (27)$$

This fit gives an rms scatter $\sigma = 0.07\,\mathrm{dex}$ on $\log_{10}(M_{\mathrm{d}})$ (with $\sim 25\,400$ dof), implying that dust mass surface densities can be inferred from 500 μm luminosity surface densities to within $\sim 20\%$. The slope is significantly sublinear, over almost three decades of 500 μm luminosity surface densities, reflecting the tendency for dust to be somewhat warmer in pixels where Σ_{Md} is high, presumably because these pixels are more likely to harbor star-forming regions. Groves et al. (2015) obtained a similar result globally for inferring gas mass from L_{500} for all KINGFISH galaxies including dwarfs (stellar mass $\leq 10^9\,M_\odot$); however, once Groves et al. (2015) considered only the more massive galaxies, the slope steepened and became approximately linear.

The rms deviation of only 0.07 dex from Eq. (27) implies that one can estimate M_{d} more reliably from $L_\nu(500\mu m)$ alone than from the total dust luminosity L_{d} and the ratio of two flux densities $L_\nu(160\mu m)$ and $L_\nu(500\mu m)$. This is because obtaining M_{d} from L_{d} using Eq. (25) in effect requires estimation of $\langle T_{\mathrm{d}}^{4+\beta}\rangle$, whereas obtaining M_{d} from $L_\nu(500\mu m)$ from (27) (with an rms of 0.16 dex) requires estimating only $\langle T_{\mathrm{d}}\rangle$, since at 500$\mu m$ the dust emission is in the Rayleigh-Jeans limit, with $L_\nu(500\mu m) \propto M_{\mathrm{d}} \times \langle T_{\mathrm{d}}\rangle$.

To estimate ISM mass from Eq. (27), the dust mass from Eq. (27) needs to be combined with a gas-to-dust

ratio as discussed in Sect. 6.6. However, this ratio depends on metallicity (see Fig. 8); thus oxygen abundance needs to be incorporated to estimate gas mass for metal poor galaxies. In any case, Fig. 16 shows that the slope between dust mass and luminosity is steeper, closer to unity, at *lower* surface brightnesses, roughly independently of wavelength. However, global integrated values of quantities such as long-wavelength IR luminosity are luminosity weighted, thus sampling preferentially *higher* surface brightnesses. Thus, our new result for resolved regions in KINGFISH galaxies is inconsistent with a strictly linear trend of dust mass with long-wavelength IR luminosity. Indeed, as noted above, a non-linear behavior would be expected since the dust in high Σ_{Md} pixels is, on average, somewhat warmer.

7. SUMMARY

Dust modeling results for 70 galaxies (61 KINGFISH galaxies, plus 9 additional galaxies present in the observed fields) are presented here. Dust is detected reliably in 62 galaxies, and upper limits are reported for the remaining 8. Tables 5 and 6 report the global galaxy photometry, and the best-fit dust parameter estimates are given in Table 9. Dust parameter maps are displayed in Figs. 17.1-17.62. The DL07 dust model successfully reproduces the dust SEDs over the wide variety of environments present in the KINGFISH sample.

Long-wavelength imaging can be omitted in order to increase the angular resolution of the modeling, but results become unreliable if the long-wavelength coverage is insufficient. For maximum reliability, we recommend using all cameras available, including MIPS160 and SPIRE250, SPIRE350, and SPIRE500. If better angular resolution is critical, the lowest-resolution cameras (SPIRE500 and MIP160) can be left out, but estimates of dust mass become unreliable unless at least SPIRE250 is included. If SPIRE350, SPIRE500, and MIPS160 are not included, the DL07 model dust masses can be low by as much as a factor 0.8, or high by as much as a factor 2 (see Figs. 20); the median factor is 1.25. q_{PAH} and f_{PDR} estimates are fairly insensitive to the camera combination used, so they can be obtained reliably without $\lambda > 250\mu m$ photometry, provided that the signal/noise ratio is adequate.

Resolved (multipixel) and global (single-pixel) modeling generate similar estimates of M_d, q_{PAH}, and f_{PDR} when all the *Spitzer* and *Herschel* cameras are employed. The single-pixel modeling tends to slightly underestimate the total dust mass M_d by $\sim 13\%$ (see Fig. 21).

Our analysis shows that q_{PAH}, the fraction of the dust mass contributed by PAHs, correlates much better with the PP04N2 estimate for O/H than for the PT estimate, strongly suggesting that PP04N2 is a better strong-line abundance estimator than the PT estimator. We find that q_{PAH} appears to increase monotonically with increasing metallicity, with q_{PAH} varying linearly with

log(O/H) for $12 + \log_{10}(O/H)_{PP04N2} > 7.94$ (see Fig. 7b and Eq. 18).

For most star-forming galaxies with metallicity $Z \gtrsim Z_\odot$, the dust/gas ratio is close to the limiting value where nearly all of the refractory elements are locked up in grains. However, at lower metallicity, the dust/gas ratio is often well below this limiting value, consistent with what is expected from a simple toy model with accretion rate $\tau_a^{-1} \propto Z_d$ (see Fig. 8b).

The resolved regions in the KINGFISH galaxy sample show several trends with U_{min}, q_{PAH}, and mass-to-light ratios for dust emission. U_{min} can be estimated from long-wavelength flux ratios (e.g., f_{160}/f_{500}) to within a factor of two over more than two orders of magnitude in U_{min} [see Eq. (22)]. From the same flux ratio, and with a measurement of dust luminosity, dust mass can be estimated to within $\sim 50\%$ [see Eq. (25)]. Despite a variation of $\gtrsim 3$ orders of magnitude in IR surface brightness, for the adopted physical dust model it is possible to estimate dust mass from IR luminosity at $500\,\mu m$ to within $\sim 0.07\,dex$), affording an accuracy of $\sim 20\%$ [see Eq. (27)]. There are of course systematic errors coming from the choice of dust model, but these are difficult to estimate. Estimating gas mass for metal-poor galaxies requires incorporating metallicity, because of the metallicity dependence of dust-to-gas ratios. Our formulations for inferring starlight heating intensity and dust mass from flux ratios and integrated IR or monochromatic luminosities have been calibrated over $\gtrsim 22\,000$ independent regions in 62 galaxies, spanning metal-poor dwarf irregulars to grand-design spiral disks and actively star-forming LIRGs. These calibrated prescriptions are designed with the aim of facilitating comparison with high-redshift galaxies, where frequently rest-frame f_{160} and at least one longer wavelength flux are available.

REFERENCES

Alatalo, K., Blitz, L., Young, L. M., et al. 2011, ApJ, 735, 88

Alatalo, K., Lacy, M., Lanz, L., et al. 2015, ApJ, 798, 31

Andrews, B. H., & Martini, P. 2013, ApJ, 765, 140

Aniano, G., Draine, B. T., Gordon, K. D., & Sandstrom, K. M. 2011, PASP, 123, 1218

Aniano, G., Draine, B. T., Calzetti, D., et al. 2012, ApJ, 756, 46

Asano, R. S., Takeuchi, T. T., Hirashita, H., & Inoue, A. K. 2013, Earth, Planets, and Space, 65, 213

Asplund, M., Grevesse, N., Sauval, A. J., & Scott, P. 2009, ARA&A, 47, 481

Bajaja, E., van der Burg, G., Faber, S. M., et al. 1984, A&A, 141, 309

Berg, D. A., Skillman, E. D., Croxall, K. V., et al. 2015, ApJ, 806, 16

Boselli, A., Lequeux, J., Sauvage, M., et al. 1998, A&A, 335, 53

Bot, C., Ysard, N., Paradis, D., et al. 2010, A&A, 523, A20

Calzetti, D., Wilson, G. W., Draine, B. T., et al. 2018, ApJ, 852, 106

Chastenet, J., Sandstrom, K., Chiang, I.-D., et al. 2019, ApJ, 876, 62

Chiang, I. D., Sandstrom, K. M., Chastenet, J., et al. 2018, ApJ, 865, 117

Corbelli, E., Bianchi, S., Cortese, L., et al. 2012, A&A, 542, A32

Croxall, K. V., Pogge, R. W., Berg, D. A., Skillman, E. D., & Moustakas, J. 2016, ApJ, 830, 4

Dalcanton, J. J., Fouesneau, M., Hogg, D. W., et al. 2015, ApJ, 814, 3

Dale, D. A., Cohen, S. A., Johnson, L. C., et al. 2009, ApJ, 703, 517

Dale, D. A., Aniano, G., Engelbracht, C. W., et al. 2012, ApJ, 745, 95

Dale, D. A., Cook, D. O., Roussel, H., et al. 2017, ApJ, 837, 90

De Cia, A., Ledoux, C., Mattsson, L., et al. 2016, A&A, 596, A97

Dellenbusch, K. E., Gallagher, John S., I., Knezek, P. M., & Noble, A. G. 2008, AJ, 135, 326

Donovan Meyer, J., Koda, J., Momose, R., et al. 2013, ApJ, 772, 107

Draine, B. T. 1990, in Astr. Soc. Pac. Conf. Ser. 12, The Evolution of the Interstellar Medium, ed. L. Blitz, 193–205

Draine, B. T. 2003, ARA&A, 41, 241

Draine, B. T. 2009, in Astr. Soc. Pac. Conf. Ser. 414, Cosmic Dust – Near and Far, ed. T. Henning, E. Grün, & J. Steinacker, 453–472

—. 2011, Physics of the Interstellar and Intergalactic Medium (Princeton, NJ: Princeton Univ. Press)

Draine, B. T., & Hensley, B. 2012, ApJ, 757, 103

Draine, B. T., & Li, A. 2007, ApJ, 657, 810

Draine, B. T., & Salpeter, E. E. 1979, ApJ, 231, 77

Draine, B. T., Dale, D. A., Bendo, G., et al. 2007, ApJ, 663, 866

Draine, B. T., Aniano, G., Krause, O., et al. 2014, ApJ, 780, 172

Eales, S., Smith, M. W. L., Auld, R., et al. 2012, ApJ, 761, 168

Edmunds, M. G. 2001, MNRAS, 328, 223

Engelbracht, C. W., Gordon, K. D., Rieke, G. H., et al. 2005, ApJL, 628, L29

Engelbracht, C. W., Rieke, G. H., Gordon, K. D., et al. 2008, ApJ, 678, 804

Esteban, C., Bresolin, F., Peimbert, M., et al. 2009, ApJ, 700, 654

Fazio, G. G., Hora, J. L., Allen, L. E., et al. 2004, ApJS, 154, 10

Galametz, M., Kennicutt, R. C., Albrecht, M., et al. 2012, MNRAS, 425, 763

Galliano, F., Hony, S., Bernard, J. P., et al. 2011, A&A, 536, A88

Giard, M., Bernard, J. P., Lacombe, F., Normand, P., & Rouan, D. 1994, A&A, 291, 239

Gordon, K. D., Meixner, M., Meade, M. R., et al. 2011, AJ, 142, 102

Griffin, M. J., Abergel, A., Abreu, A., et al. 2010, A&A, 518, L3

Groves, B. A., Schinnerer, E., Leroy, A., et al. 2015, ApJ, 799, 96

Helou, G., Roussel, H., Appleton, P., et al. 2004, ApJS, 154, 253

Hota, A., & Saikia, D. J. 2005, MNRAS, 356, 998

Hunt, L., Bianchi, S., & Maiolino, R. 2005, A&A, 434, 849

Hunt, L., Dayal, P., Magrini, L., & Ferrara, A. 2016, MNRAS, 463, 2002

Hunt, L. K., Thuan, T. X., Izotov, Y. I., & Sauvage, M. 2010, ApJ, 712, 164

Hunt, L. K., Draine, B. T., Bianchi, S., et al. 2015, A&A, 576, A33

Hunter, D. A., Ficut-Vicas, D., Ashley, T., et al. 2012, AJ, 144, 134

Israel, F. P., Wall, W. F., Raban, D., et al. 2010, A&A, 519, A67

Kennicutt, R. C., Armus, L., Bendo, G., et al. 2003, PASP, 115, 928

Kennicutt, R. C., Calzetti, D., Aniano, G., et al. 2011, PASP, 123, 1347

Kewley, L. J., & Ellison, S. L. 2008, ApJ, 681, 1183

Kobulnicky, H. A., & Kewley, L. J. 2004, ApJ, 617, 240

Leroy, A. K., Walter, F., Bigiel, F., et al. 2009, AJ, 137, 4670

Leroy, A. K., Walter, F., Sandstrom, K., et al. 2013, AJ, 146, 19

Li, Y., Bresolin, F., & Kennicutt, Jr., R. C. 2013, ApJ, 766, 17

Li, Z., Jones, C., Forman, W. R., et al. 2011, ApJ, 730, 84

Madden, S. C. 2000, New Astronomy Review, 44, 249

Makarov, D., Prugniel, P., Terekhova, N., Courtois, H., & Vauglin, I. 2014, A&A, 570, A13

Marble, A. R., Engelbracht, C. W., van Zee, L., et al. 2010, ApJ, 715, 506

Martinez-Badenes, V., Lisenfeld, U., Espada, D., et al. 2012, A&A, 540, A96

Mathis, J. S., Mezger, P. G., & Panagia, N. 1983, A&A, 128, 212

Mattsson, L., Andersen, A. C., & Munkhammar, J. D. 2012, MNRAS, 423, 26

McMullin, J. P., Waters, B., Schiebel, D., Young, W., & Golap, K. 2007, Astronomical Society of the Pacific Conference Series, Vol. 376, CASA Architecture and Applications, ed. R. A. Shaw, F. Hill, & D. J. Bell, 127

Moustakas, J., Kennicutt, R. C., Tremonti, C. A., et al. 2010, ApJS, 190, 233

Muñoz-Mateos, J. C., Gil de Paz, A., Boissier, S., et al. 2009, ApJ, 701, 1965

Ott, S. 2010, in Astronomical Society of the Pacific Conference Series, Vol. 434, Astronomical Data Analysis Software and Systems XIX, ed. Y. Mizumoto, K.-I. Morita, & M. Ohishi, 139–142

Pellegrini, E. W., Smith (PI, J. D., Wolfire, M. G., et al. 2013, ApJL, 779, L19

Pettini, M., & Pagel, B. E. J. 2004, MNRAS, 348, L59

Pilbratt, G. L., Riedinger, J. R., Passvogel, T., et al. 2010, A&A, 518, L1

Pilyugin, L. S., Grebel, E. K., & Kniazev, A. Y. 2014, AJ, 147, 131

Pilyugin, L. S., & Thuan, T. X. 2005, ApJ, 631, 231

Pilyugin, L. S., Thuan, T. X., & Vílchez, J. M. 2006, MNRAS, 367, 1139

—. 2007, MNRAS, 376, 353

Planck Collaboration, Ade, P. A. R., Aghanim, N., et al. 2011, A&A, 536, A17

—. 2016, A&A, 586, A132

Poglitsch, A., Waelkens, C., Geis, N., et al. 2010, A&A, 518, L2

Povich, M. S., Stone, J. M., Churchwell, E., et al. 2007, ApJ, 660, 346

R Core Team. 2014, R: A Language and Environment for Statistical Computing, R Foundation for Statistical Computing, Vienna, Austria

Relaño, M., Kennicutt, R., Lisenfeld, U., et al. 2016, A&A, 595, A43

Rémy-Ruyer, A., Madden, S. C., Galliano, F., et al. 2013, A&A, 557, A95

—. 2014, A&A, 563, A31

Rieke, G. H., Young, E. T., Engelbracht, C. W., et al. 2004, ApJS, 154, 25

Roche, P. F., Aitken, D. K., Smith, C. H., & Ward, M. J. 1991, MNRAS, 248, 606

Roussel, H. 2013, PASP, 125, 1126

Roussel, H., Helou, G., Smith, J. D., et al. 2006, ApJ, 646, 841

Sandstrom, K. M., Leroy, A. K., Walter, F., et al. 2013, ApJ, 777, 5

Scoville, N., Aussel, H., Sheth, K., et al. 2014, ApJ, 783, 84

Scoville, N., Sheth, K., Aussel, H., et al. 2016, ApJ, 820, 83

Scoville, N., Lee, N., Vanden Bout, P., et al. 2017, ApJ, 837, 150

Skibba, R. A., Engelbracht, C. W., Dale, D., et al. 2011, ApJ, 738, 89

Storchi-Bergmann, T., Calzetti, D., & Kinney, A. L. 1994, ApJ, 429, 572

Strickland, D. K., Heckman, T. M., Colbert, E. J. M., Hoopes, C. G., & Weaver, K. A. 2004, ApJS, 151, 193

Sturm, E., Lutz, D., Tran, D., et al. 2000, A&A, 358, 481

Utomo, D., Chiang, I. D., Leroy, A. K., Sandstrom, K. M., & Chastenet, J. 2019, ApJ, 874, 141

Vagshette, N. D., Pandge, M. B., Pandey, S. K., & Patil, M. K. 2012, NewA, 17, 524

van Zee, L., Haynes, M. P., & Salzer, J. J. 1997, AJ, 114, 2479

Vílchez, J. M., Relaño, M., Kennicutt, R., et al. 2019, MNRAS, 483, 4968

Walter, F., Brinks, E., de Blok, W. J. G., et al. 2008, AJ, 136, 2563

Weingartner, J. C., & Draine, B. T. 1999, ApJ, 517, 292

—. 2001a, ApJ, 548, 296

—. 2001b, ApJ, 553, 581

Werner, M. W., Roellig, T. L., Low, F. J., et al. 2004, ApJS, 154, 1

Zhukovska, S., Dobbs, C., Jenkins, E. B., & Klessen, R. S. 2016, ApJ, 831, 147

APPENDIX

A. RESOLVED DUST PARAMETER MAPS FOR KINGFISH GALAXIES

As described in the text, each galaxy where we have a positive dust detection has two figures: the first (a) shows the model done at MIPS160 resolution, using data from all cameras (IRAC, MIPS, PACS, and SPIRE) cameras. This is our "gold standard" modeling. The second (b) shows a model at SPIRE250 resolution, using IRAC, MIPS24, PACS, and SPIRE250 cameras (i.e., omitting MIPS70, MIPS160, SPIRE350, SPIRE500). This latter modeling, while able to resolve smaller scale structures in the galaxies, is overall less reliable.

Figures 17.1-17.62 each have twelve panels. For each of the resolutions. the top row is a map of dust luminosity surface density Σ_{L_d} (left), dust surface density Σ_{M_d} (center), and the model SED (right). The lower row shows the starlight intensity parameter $U_{\mathrm{min,DL07}}$ (left), the PAH abundance parameter q_{PAH} (center), and the PDR fraction f_{PDR} (left). The dust luminosity surface density Σ_{L_d} is shown for the full field, with the white contour showing the minimum surface brightness $\Sigma_{Ld,\mathrm{min}}$ below which we do not attempt to model the emission. Maps of derived quantities (Σ_{M_d}, U_{min}, q_{PAH}, and f_{PDR}) are limited to the "galaxy mask" region with $\Sigma_{L_\mathrm{d}} > \Sigma_{Ld,\mathrm{min}}$. In the SED plot, the observed photometry is represented by rectangular boxes (*Spitzer* (IRAC, MIPS) in red; *Herschel* (PACS, SPIRE) in blue) showing $\pm1\sigma$ uncertainties. The black line is a single-pixel DL07 model that seeks to reproduce the observed SED, with different components shown. The values of U_{min} and M_d in the label are for the DL07 model before renormalization. The cyan line is the stellar contribution, the dark red line is the emission from dust heated by the power-law U distribution, and the dark green line is emission from dust heated by $U = U_{\mathrm{min}}$.

Figures 17.1-17.5 are shown below as examples. This paper with a complete figure set is available at http://www.astro.princeton.edu/~draine/KFdust/KFdust_full.pdf

Fig. Set 17.
Dust Maps for 62 Galaxies
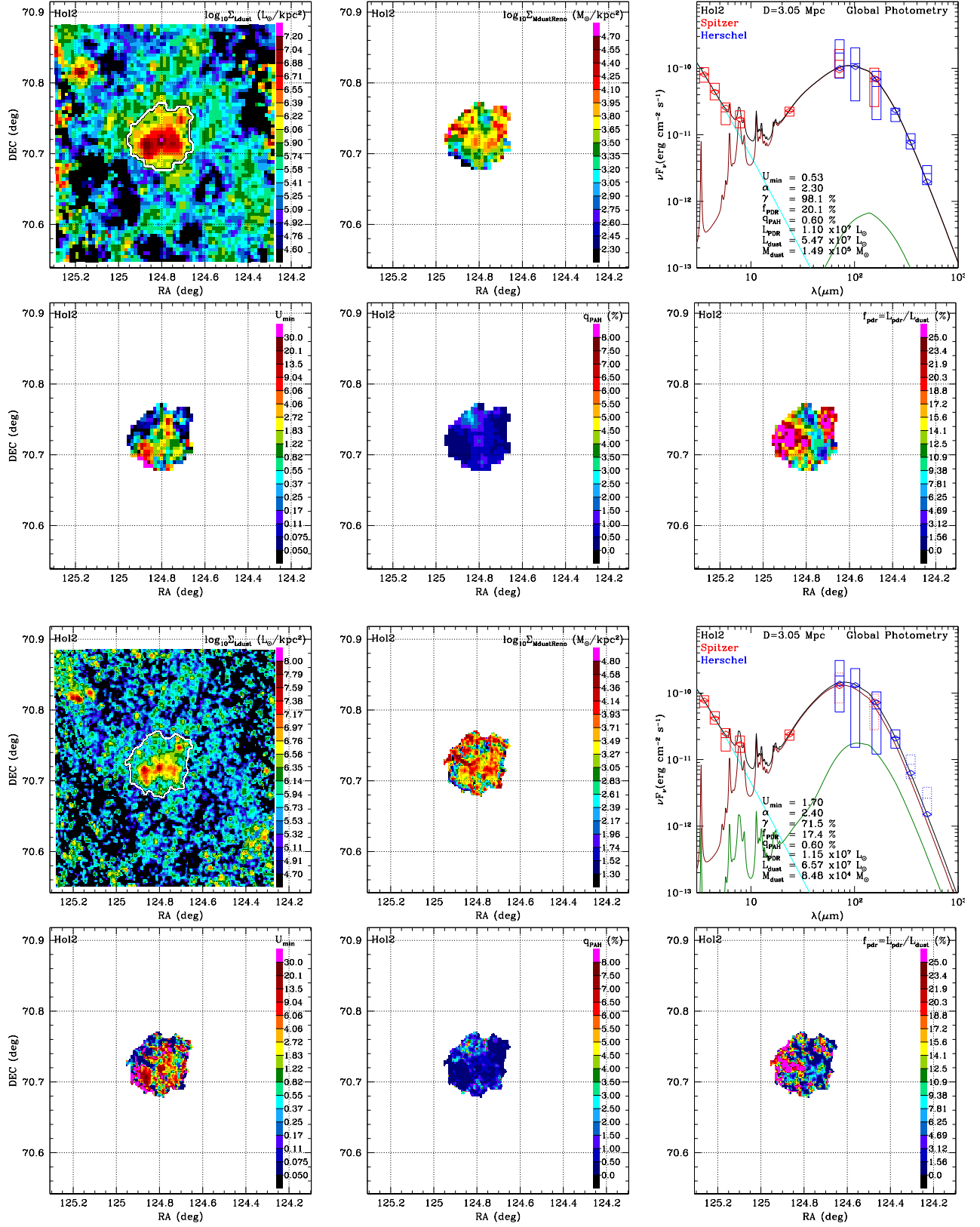
Figure 17.1 Hol2: Model results at M160 PSF (rows 1 and 2) and at S250 PSF (rows 3 and 4). Dust luminosity per area Σ_{Ld} (column 1, rows 1 and 3) is shown for entire field, with adopted galaxy mask boundary in white. Dust mass per area Σ_{Md} (column 2, rows 1 and 3) is after renormalization (see text). $U_{\mathrm{min,DL07}}$, q_{PAH} and f_{PDR} are shown in rows 2 and 4. The global SED (column 3, rows 1 and 3) is shown for single-pixel modeling, with contributions from dust heated by U_{min} (green), dust heated by $U > U_{\mathrm{min}}$ (red) and starlight (cyan); values of U_{min} and M_{d} in the figure label are for the DL07 model before renormalization. *Herschel* (blue rectangles) and *Spitzer* (red rectangles) photometry is shown; vertical extent is $\pm 1\sigma$. Diamonds show the band-convolved flux for the model.
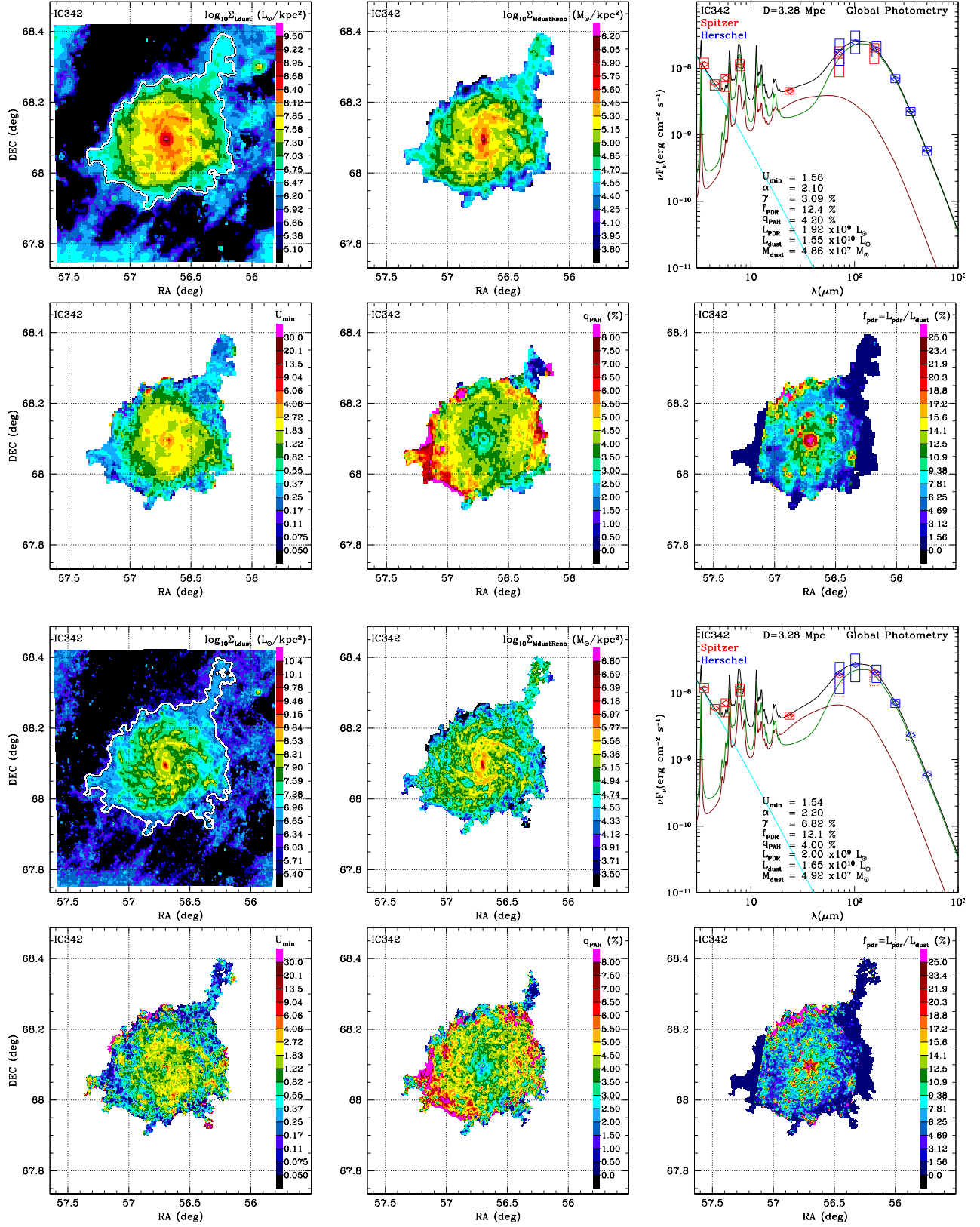
Figure 17.2 As in Figure 17.1, but for IC342. The q_{PAH} map is truncated to the NW because $8\mu m$ imaging was unavailable.

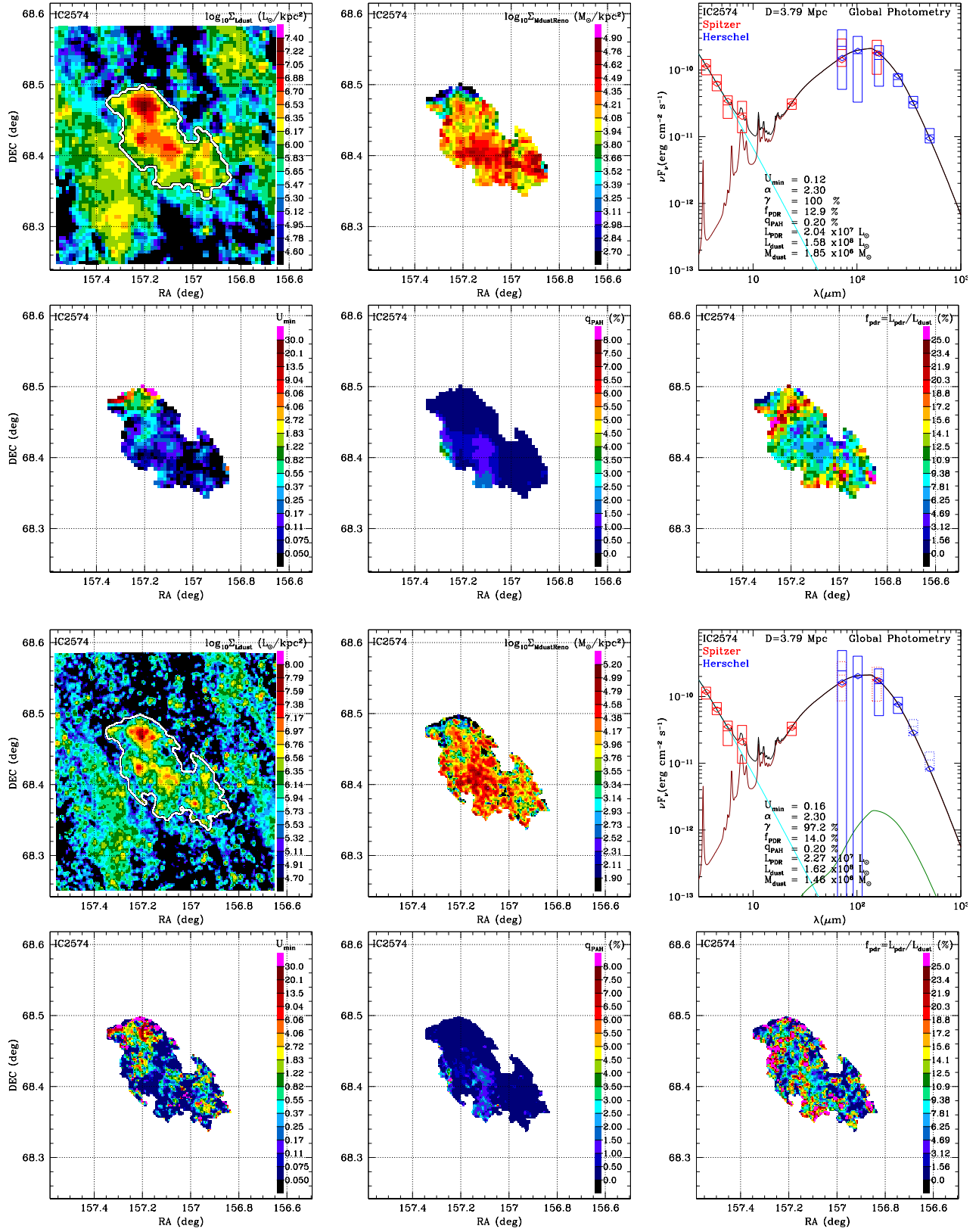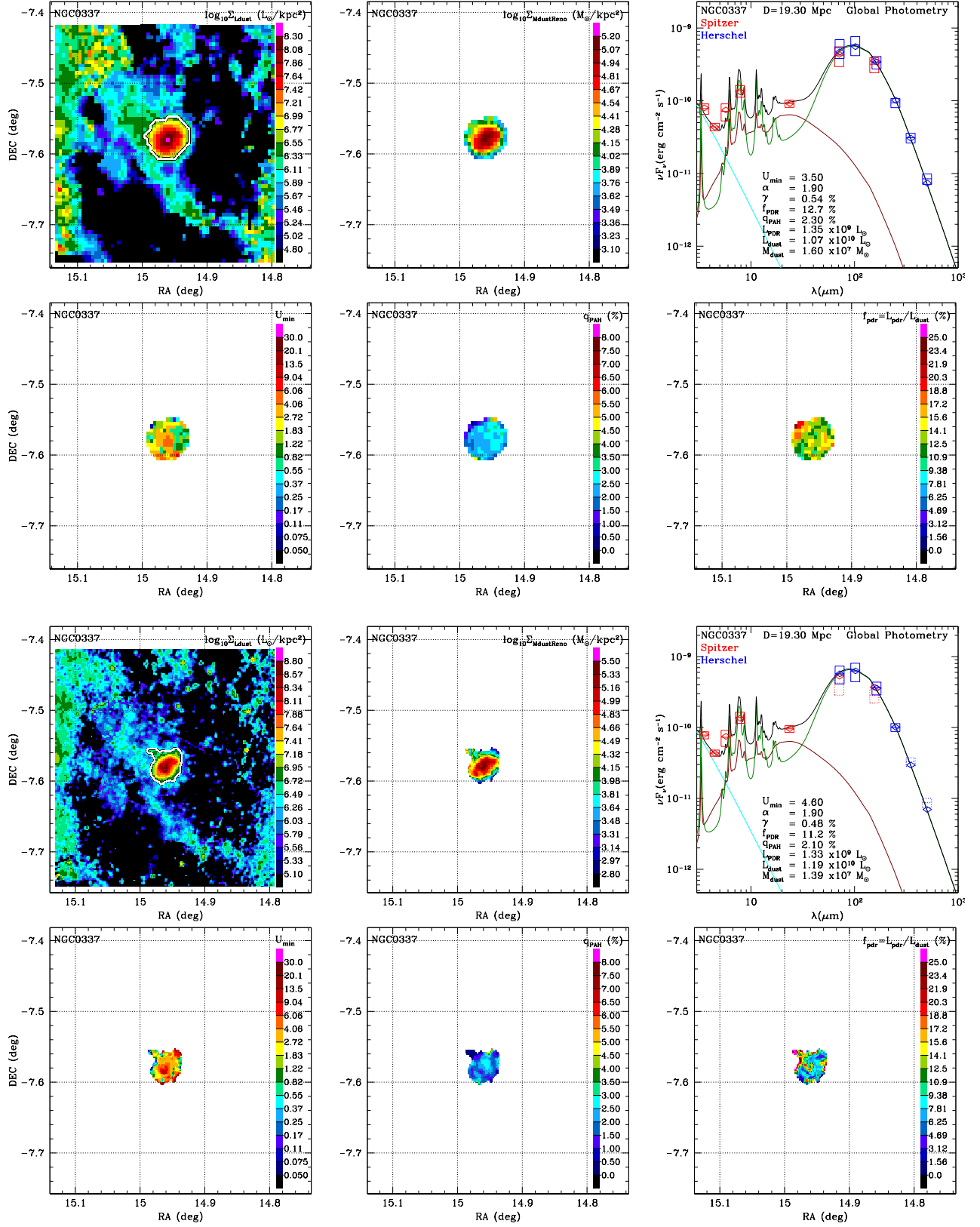**Figure 17.3** As in Figure 17.1, but for IC2574.

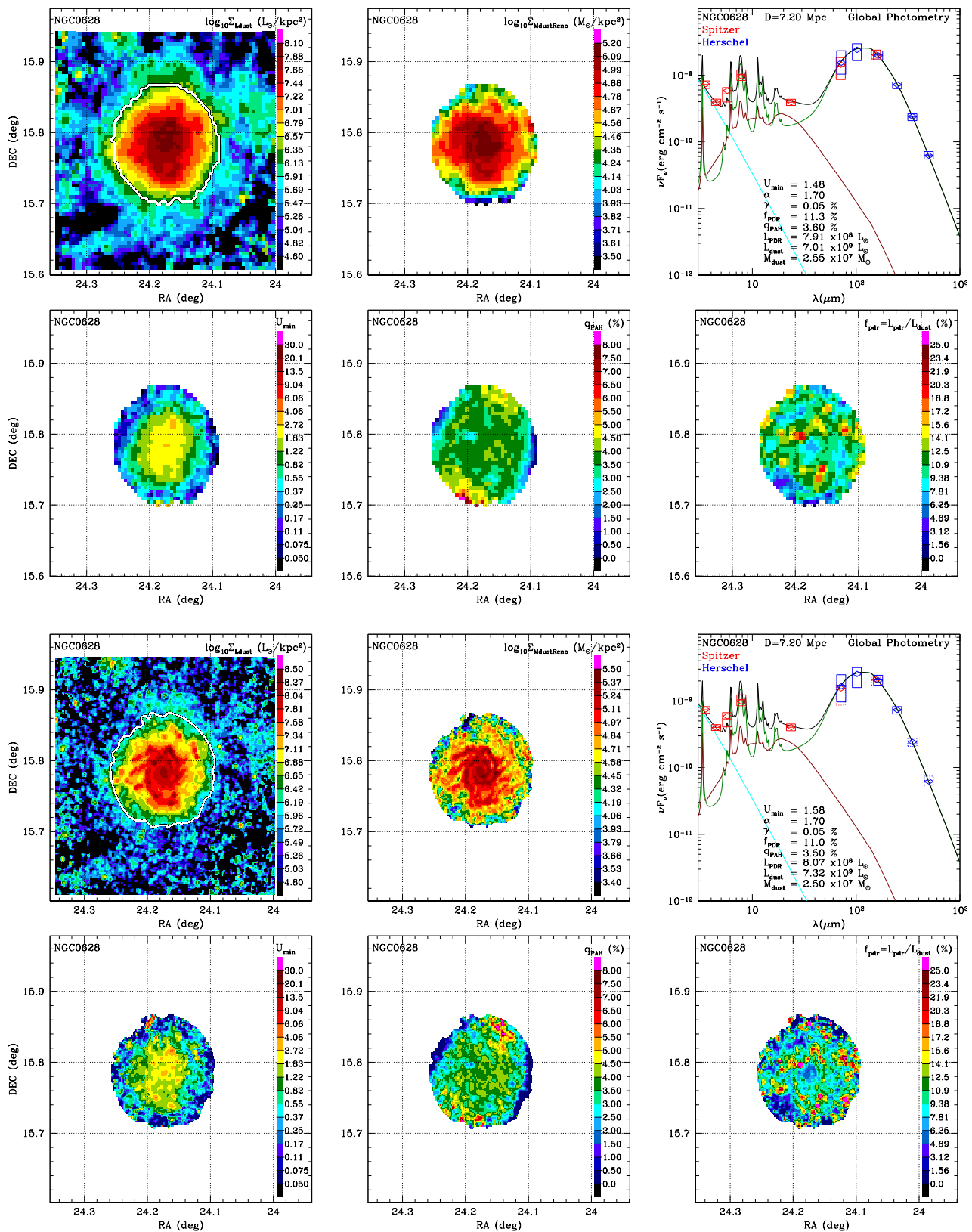**Figure 17.4** As in Figure 17.1, but for NGC0337.

Figure 17.5 As in Figure 17.1, but for NGC 0628 = M74.

B. CASES WITH 3σ UPPER LIMITS FOR DUST MASS

Eight galaxies in the KINGFISH sample five dwarfs (DDO053, DDO154, DDO165, Hol1, and M81dwB) and three ellipticals (NGC0584, NGC0855, and NGC1404) yield upper limits on the dust mass from our modeling. In these cases, the signal from the galaxy in the far-IR is of comparable magnitude to the contamination from background galaxies, leading to uncertain dust mass measurements.

For the 3 elliptical galaxies, we employ a Σ_{Ld}-based mask that roughly coincides with the optical galaxy. To obtain an upper limit on the dust mass in the case of these non-detections, we randomly shift the mask around in the M160 resolution dust mass image, avoiding overlap with the original mask, and remeasure the total dust mass. We construct a distribution of these "background" dust mass measurements to obtain a mean and standard deviation. In all galaxies mentioned above, the mean of the "background" dust mass values is positive, as would be expected due to the real signal at far-IR wavelengths from unidentified background sources ("confusion noise"). The measured dust mass at the expected galaxy location is within $\sim 1\sigma$ of the mean. In the text and Table 11 we provide the 3σ upper limit on the dust mass generated with this procedure.

The definition of the galaxy mask itself is also potentially affected by confusion noise. In the case of the dwarf galaxies, we use the H I observations from THINGS and Little THINGS to create an alternative galaxy mask, based on a cut at an H I column density of $10^{20}\,\mathrm{cm}^{-2}$ from the H I image convolved to M160 resolution. The H I-based galaxy mask is typically somewhat larger than that defined by the dust luminosity surface density cut. We apply the same procedure described above to obtain the background mean and standard deviation.

Table 11. Dust Upper Limits

Galaxy	$M_{\mathrm{d}}(M_{\odot})$	method
DDO053	$< 2.1 \times 10^5$	H I mask
DDO154	$< 6.1 \times 10^5$	H I mask
DDO165	$< 5.2 \times 10^5$	H I mask
Hol1	$< 6.7 \times 10^5$	H I mask
M81dwB	$< 8.1 \times 10^4$	H I mask
NGC0584	$< 1.6 \times 10^6$	Σ_{Ld} mask
NGC0855	$< 1.0 \times 10^6$	Σ_{Ld} mask
NGC1404	$< 2.0 \times 10^6$	Σ_{Ld} mask

Table 11 and Figures 18.1-18.8 provide the results of this procedure. Table 11 lists the 3σ upper limits for each galaxy using the H I-based masks for the dwarfs and the dust luminosity surface density masks (as described in the text) for the ellipticals. Histograms of the dust masses from the randomly shifted masks are shown in Figures 18.1-18.8. We note that the dust mass limits from this procedure are expected to be very conservative. Higher S/N could be obtained by a careful treatment of the integrated photometry for each galaxy taking the confusion noise into account.

Figure 18.1 (DDO053) and Figure 18.5 (NGC0584) are shown below as examples. This paper with a complete figure set is available at

http://www.astro.princeton.edu/~draine/KFdust/KFdust_full.pdf

Fig. Set 18. 8 Galaxies with Upper Limits for Dust Mass: DDO053, DDO154, DDO165, Hol1, M81dwB, NGC0584, NGC0855, NGC1404
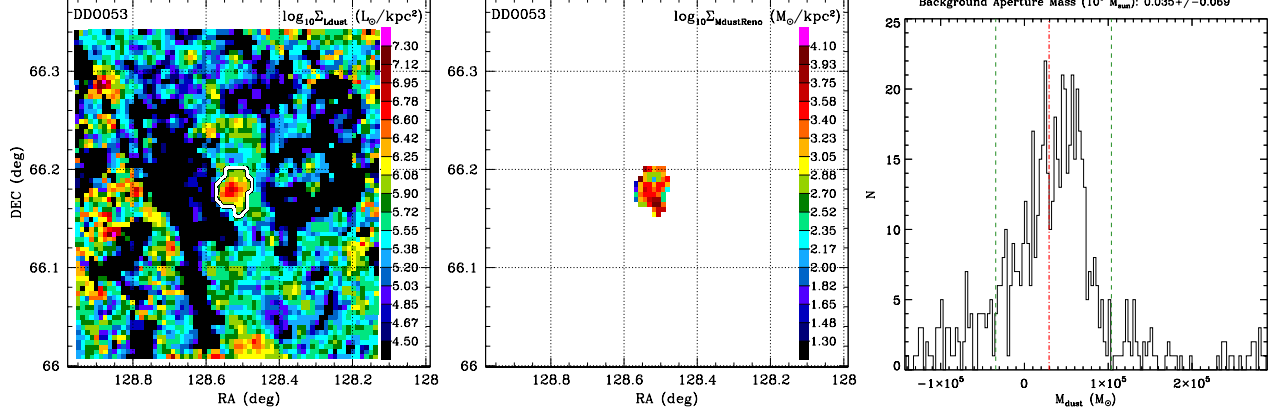
Figure 18.1 DDO053: Left: Σ_{Ld} map; contours: $\Sigma_{Ld,\min} = 0.6 L_\odot\,\mathrm{pc}^{-2}$. Center: Σ_{Md} map within the galaxy mask. Right: histogram of M_d for H I-based mask, shifted randomly. Red dot-dashed line: M_d for mask centered on galaxy. 68% of random masks give M_d between green dashed lines.
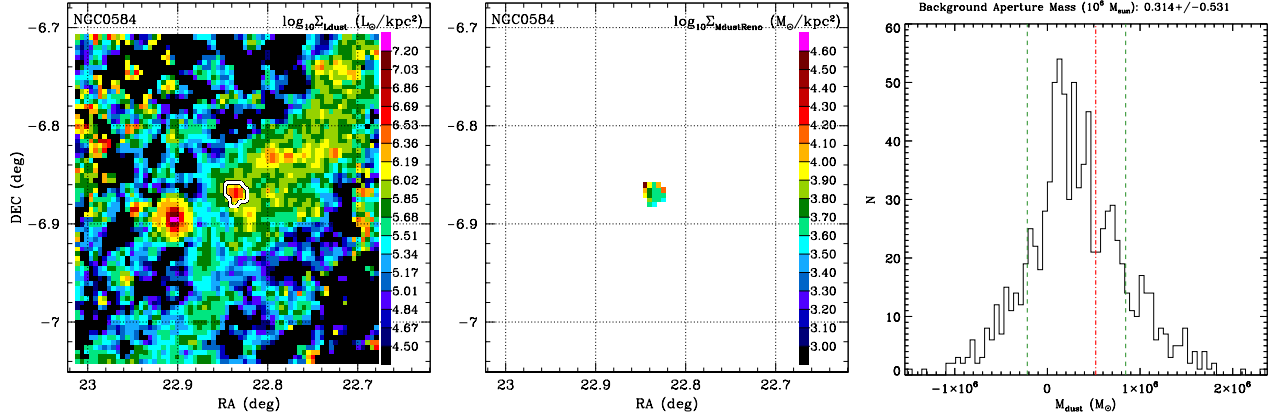
Figure 18.5 NGC0584: Left: Σ_{Ld} map; contours: $\Sigma_{Ld,\min} = 0.6 L_\odot\,\mathrm{pc}^{-2}$. Center: Σ_{Md} map within the galaxy mask. Right: histogram of M_d for Σ_{Ld}-based mask, shifted randomly. Red dot-dashed line: M_d for mask centered on galaxy. 68% of random masks give M_d between green dashed lines.

C. ON-LINE KINGFISH DATA AND DUST MODELS

The processed KINGFISH imaging and dust models are available online at http://www.astro.princeton.edu/~draine/KFdust/KFdustsite/

Here we briefly describe the types of data that are available there.

For each of the 70 galaxies (61 KINGFISH galaxies + 9 "extras") we provide results for resolved modeling at 4 different resolutions: M160, S500, S350, and S250. For each case, we use all compatible cameras (see Table 4). FITS files of the following maps are provided:

- Dust mass surface density Σ_{Md} (renormalized).

- Dust luminosity per unit projected area Σ_{Ld}.

- PAH mass fraction q_{PAH}.

- $U_{\min,\mathrm{DL07}}$ = minimum starlight intensity parameter for the DL07 model. The renormalized $U_{\min}$ can be obtained from $U_{\min,\mathrm{DL07}}$ using Eq. (16).

- $\bar{U}_{\mathrm{DL07}}$ = mean starlight intensity parameter for the DL07 model. The renormalized $\overline{U}$ can be obtained from $\bar{U}_{\mathrm{DL07}}$ using Eq. (15).

- f_{PDR} = fraction of the total starlight heating of dust taking place in subregions where $U > 10^2$.

- global SED for the dust model.

For each case, the data in the FITS files are limited to the "galaxy mask" defined by $\Sigma_{Ld} > \Sigma_{Ld,\min}$, where $\Sigma_{Ld,\min}$ for each galaxy is given in Table 2.

D.   DEPENDENCE OF MODEL RESULTS ON PSF USED AND WAVELENGTH COVERAGE

Obviously, one would like to model the dust emission with the best angular resolution that is feasible. Some of the cameras (e.g., PACS160) have small PSFs, which would seem to allow observations and modeling with high angular resolution. However, deciding to use a small PSF means not being able to use data from cameras with larger PSFs, which both reduces the amount of redundant data (e.g., MIPS70 and MIPS160) and limits the wavelength coverage by preventing use of the longer wavelength cameras (e.g., SPIRE500). In addition, use of a smaller PSF implies a lower signal/noise ratio, which is a limiting factor in low surface brightness regions.

Here we examine the degree to which derived dust and starlight parameters are sensitive to the choice of PSF. We also compare the results obtained from the resolved modeling and those from global photometry.

D.1.   *Comparison of modeling at S250 resolution with the gold standard (M160)*

Figure 19 shows the comparison of the dust parameter estimates obtained from models using the S250 PSF (18.2″FWHM) with parameters estimated from (our "gold standard") modeling using all cameras (IRAC, MIPS, PACS, SPIRE) and the M160 PSF (39″FWHM).

The results for L_{d} and M_{d} at S250 resolution appear to be quite robust: the median change in L_{d} is only 5%, which may be due in part to calibration differences between MIPS160 and PACS160, with MIPS160 data being used only in the M160 PSF modeling. M_{d} shows more variation: with a median change of 25%; this is likely because loss of SPIRE350 and SPIRE500 may allow modeling at the S250 PSF to include a bit more cool dust than is actually present. However, it is gratifying that the median change is only 25%, indicating that the DL07 model is relatively good at "predicting" $\lambda > 300\mu$m emission using data shortward of 300μm. However, in some cases the dust mass is overestimated by as much as a factor of 2 (see Fig. 20), and we therefore recommend using M160 resolution modeling rather than the riskier S250 PSF.

D.2.   *Dust mass estimates at different resolutions*

Figure 20 shows the comparison of the dust mass estimates for 4 different resolutions and camera combinations. The compared resolutions are

- M160 (the "gold standard") uses all the cameras (IRAC, MIPS, PACS, SPIRE) at the MIPS160 PSF; this is taken to be our best estimate for M_{d}

- S500: IRAC, MIPS24, MIPS70, PACS, and SPIRE at the SPIRE500 PSF.

- S350: IRAC, MIPS24, MIPS70, PACS, SPIRE250, and SPIRE350 at the SPIRE350 PSF.

- S250: IRAC, MIPS24, PACS, and SPIRE250 at the SPIRE250 PSF.

- P160: IRAC, MIPS24, and PACS at the PACS160 PSF. This is the riskiest PSF we are willing to consider.

For each resolution, Fig. 20 shows a histogram of the galactic total dust mass estimates divided by the gold standard estimate.

We observe that dust mass discrepancies can be large, with the errors and bias increasing as fewer cameras are used, and long-wavelength data are lost. The S500 case (coverage out to 500μm, a PSF that is not much smaller than the M160 PSF, but no MIPS160 photometry) gives dust mass estimates that are close to our gold standard estimate, with a median ratio of 1.21. However, there are a few outliers where M_{d} appears to be overestimated by as much a factor of 2. These are all galaxies with very weak dust emission and low signal/noise data, where loss of the data from one camera (MIPS160) causes a significant change in the apparent SED.

The systematic bias in M_{d} as well as the scatter both increase as we move to smaller PSFs (S350, S250, P160). At P160 resolution, fully 25% of the cases have M_{d} *under*-estimated by a factor of 2 or more.

On balance, it appears that modeling at S250 resolution is reasonable, although slightly risky – there is a significant chance that the dust mass may be overestimated or underestimated by a factor 1.5 or more. S350 resolution is safer, and S500 even better.
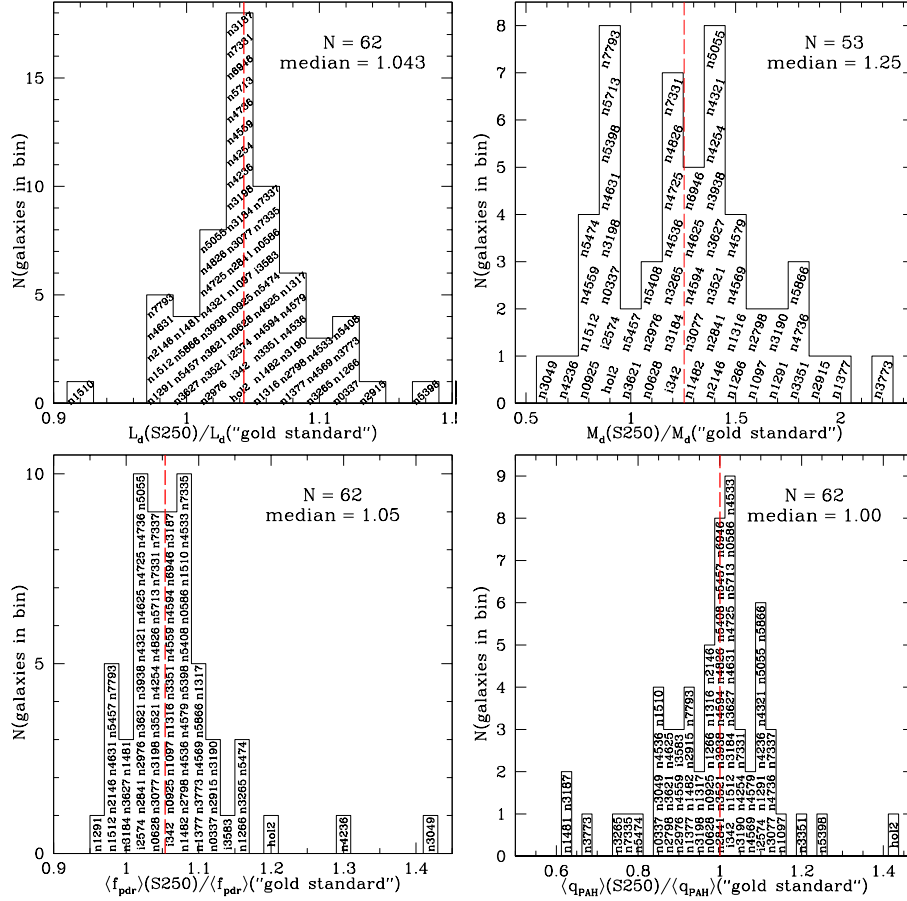
Figure 19. Comparison of modeling with the S250 PSF to results obtained with the M160 PSF (the "gold standard"). With S250 modeling, the dust mass tends to be slightly overestimated; the median overestimation is ~25%.

### D.3. *Modeling using only global photometry (single-pixel)*

The KINGFISH galaxies are close ($D < 30\,\mathrm{Mpc}$) and large enough that they can be resolved using *Herschel* Space Telescope. When studying galaxies at larger distances, only their global photometry may be available. Here we compare our dust mass estimates using resolved imaging and multipixel modeling with "single-pixel" modeling that makes use of only the global SED. We recall that the dust modeling is not a linear process, and differences in parameter estimates are to be expected.

Figure 21 shows the ratio of the dust model parameter estimates from fitting global photometry (a "single pixel" model) versus our "gold standard" multipixel modeling at M160 resolution, where each pixel is modeled separately. In both cases we use all cameras: IRAC, MIPS, PACS and SPIRE. We observe that L_d is very reproducible, with the single-pixel luminosity estimate differing from the multipixel result by only a few percent.

The dust mass estimate is probably most important, and is found to be moderately robust: for 75% of the cases, the single-pixel modeling obtains a mass estimate within 25% of the resolved multipixel analysis. Thus dust mass estimates for unresolved distant galaxies should be reliable, assuming only that the photometry covers a suitable range of wavelengths (rest-frame wavelengths $50 \lesssim \lambda \lesssim 300\mu\mathrm{m}$), with an adequate signal/noise ratio.

The $\langle f_\mathrm{PDR} \rangle$ and $\langle q_\mathrm{PAH} \rangle$ estimates are both quite robust, with the single pixel results agreeing with the multipixel analysis to within ~5% in most cases.
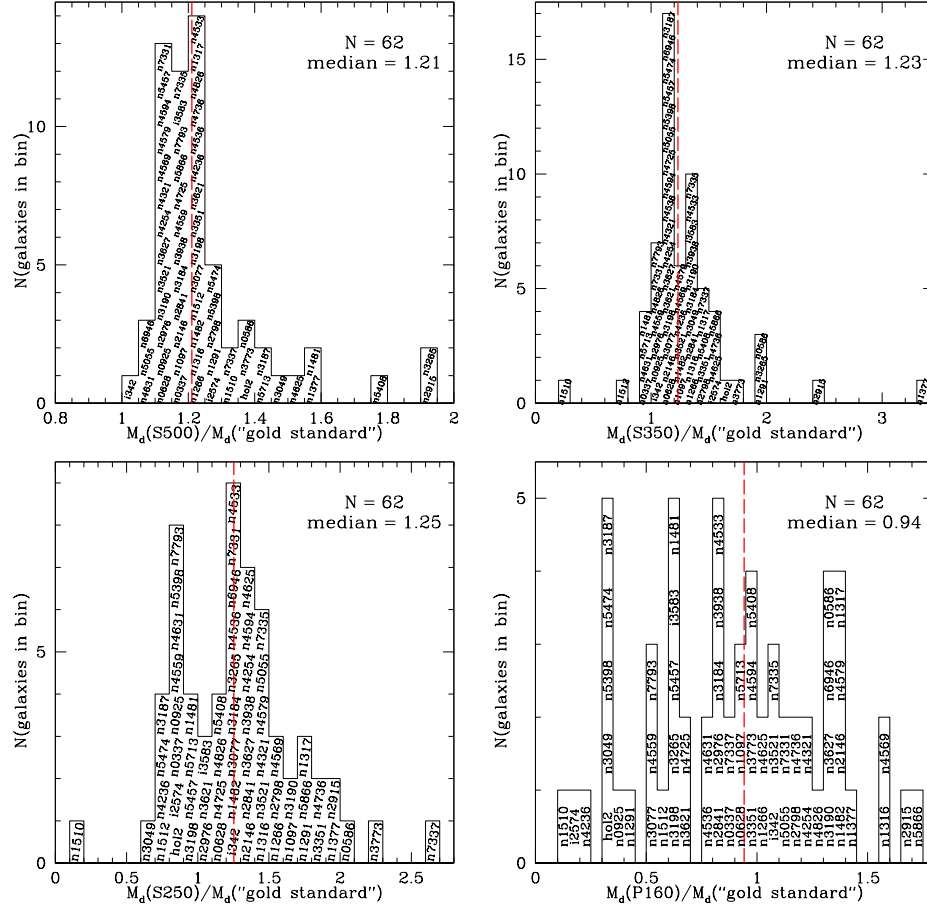
Figure 20. Comparison of estimates for dust mass M_d obtained from multipixel modeling with different PSFs and camera combinations. The "gold standard" refers to modeling with the M160 PSF and all cameras. Here we compare M_d obtained with the S500, S350, S250, and P160 PSFs (see Table 4). Because of the limited wavelength coverage, and lower signal/noise ratio, for the P160 PSF the dust mass can be in error by up to a large factor: 10/62 cases underestimate the dust mass by more than a factor of 2, and 2/62 cases by more than a factor of 5.
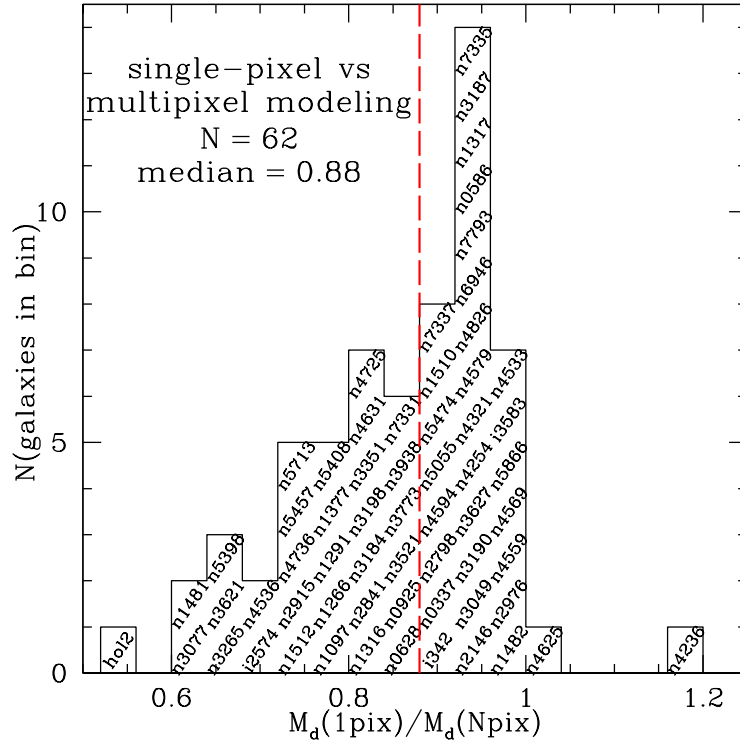
Figure 21. Dust mass estimation using global (single-pixel) modeling versus sum over resolved (multi-pixel) modeling at M160 resolution. Single-pixel modeling estimates the total dust mass to within a factor of 2 in the worst case (Holmberg II), but for ~70% of the cases the single-pixel mass is within 25% of the multipixel mass.